Received: 23 May 2023 | Revised: 18 July 2023 | Accepted: 27 July 2023

DOI: 10.1002/pro.4742

RESEARCH ARTICLE

THE PROTEIN SOCIETY WILEY

Promoting the activity of a receptor tyrosine phosphatase with a novel pH-responsive transmembrane agonist inhibits cancer-associated phenotypes

Sophie Rizzo[1] | **Eden Sikorski**[1] | **Soohyung Park**[2] | **Wonpil Im**[1,2] | **Victor Vasquez-Montes**[3] | **Alexey S. Ladokhin**[3] | **Damien Thévenin**[1]

[1]Department of Chemistry, Lehigh University, Bethlehem, Pennsylvania, USA

[2]Department of Biological Sciences, Lehigh University, Bethlehem, Pennsylvania, USA

[3]Department of Biochemistry and Molecular Biology, The University of Kansas Medical Center, Kansas City, Kansas, USA

Correspondence
Damien Thévenin, Department of Chemistry, Lehigh University, Bethlehem, PA 18015, USA.
Email: damien.thevenin@lehigh.edu

Funding information
National Institute of General Medical Sciences, Grant/Award Numbers: R01GM139998, R01GM126778; National Science Foundation, Grant/Award Number: 2111728

Review Editor: Aitziber L. Cortajarena

Abstract

Cell signaling by receptor protein tyrosine kinases (RTKs) is tightly controlled by the counterbalancing actions of receptor protein tyrosine phosphatases (RPTPs). Due to their role in attenuating the signal-initiating potency of RTKs, RPTPs have long been viewed as therapeutic targets. However, the development of activators of RPTPs has remained limited. We previously reported that the homodimerization of a representative member of the RPTP family (protein tyrosine phosphatase receptor J or PTPRJ) is regulated by specific transmembrane (TM) residues. Disrupting this interaction by single point mutations promotes PTPRJ access to its RTK substrates (e.g., EGFR and FLT3), reduces RTK's phosphorylation and downstream signaling, and ultimately antagonizes RTK-driven cell phenotypes. Here, we designed and tested a series of first-in-class pH-responsive TM peptide agonists of PTPRJ that are soluble in aqueous solution but insert as a helical TM domain in lipid membranes when the pH is lowered to match that of the acidic microenvironment of tumors. The most promising peptide reduced EGFR's phosphorylation and inhibited cancer cell EGFR-driven migration and proliferation, similar to the PTPRJ's TM point mutations. Developing tumor-selective and TM-targeting peptide binders of critical RPTPs could afford a potentially transformative approach to studying RPTP's selectivity mechanism without requiring less specific inhibitors and represent a novel class of therapeutics against RTK-driven cancers.

KEYWORDS

allosteric modulation, cancer, epidermal growth factor receptor (EGFR), peptide binder, receptor protein tyrosine phosphatase (RPTP), receptor tyrosine kinase (RTK), transmembrane domain oligomerization, tumor acidity

1 | INTRODUCTION

Protein tyrosine phosphorylation is essential for initiating and propagating cell signal transduction in response to external stimuli (Manning et al., 2002; Ubersax & Ferrell Jr, 2007). The magnitude and duration of tyrosine phosphorylation are tightly regulated by the counterbalancing actions of receptor tyrosine kinases (RTKs) and receptor

protein tyrosine phosphatases (RPTPs). Indeed, RPTPs dephosphorylate regulatory tyrosine residues on RTKs to attenuate their signal-initiating potency (Hunter, 2009; Tonks, 2013). It is now recognized that disrupted RTKs and RPTPs activity through oncogenic mutations results in aberrant protein tyrosine phosphorylation and is implicated in many cancer types (Cohen & Alessi, 2013; He et al., 2014; Libermann et al., 1985; Mok, 2011; Spano et al., 2005). Accordingly, targeted small molecule inhibitors and antibodies have been developed to suppress the oncogenic activity of RTKs, such as the epidermal growth factor receptor (EGFR). While gefitinib and cetuximab can be highly effective, at least initially (Ercan et al., 2012; Furcht et al., 2013; Lazzara et al., 2010), acquired resistance can arise through gatekeeper mutations or bypass signaling via alternative RTKs (Hata et al., 2016; Niederst & Engelman, 2013).

On the other hand, several RPTPs have been identified as suppressors of many tumor types, including colon, lung, breast, and thyroid (Iuliano et al., 2004; Keane et al., 1996; Nunes-Xavier et al., 2013; Ruivenkamp et al., 2002; Ruivenkamp et al., 2003). Therefore, promoting the phosphatase activity of RPTPs represents a possible alternative to reverse malignant phenotypes driven by aberrant RTK signaling and overcome common acquired resistance mechanisms. While there are clear advantages in enhancing RPTPs tumor-suppressing activity toward dysregulated RTKs (Farrington et al., 2020), allosteric modulators of RPTPs remain underdeveloped due to a gap in knowledge of their structure–function relationship.

In contrast to their RTK counterparts, the activity of RPTPs appears to be suppressed by homodimerization (Barr et al., 2009; Hower et al., 2009; Jiang et al., 1999). We previously reported that specific transmembrane (TM) domain interactions stabilize the homodimerization of protein tyrosine phosphatase receptor J (PTPRJ) (Bloch et al., 2019), a relevant tumor suppressor and essential down-regulator of growth factor signaling, including PDGFβR (Jandt et al., 2003; Kovalenko et al., 2000; Petermann et al., 2011), VEGFR (Lampugnani et al., 2003; Patel et al., 2012), METR (Lampugnani et al., 2003; Palka et al., 2003), EGFR (Avraham & Yarden, 2011; Tarcic et al., 2009), and FLT3b (Arora et al., 2011; Böhmer et al., 2013). We identified the TM residues G979, G983, and G987 as major mediators of PTPRJ's self-association through a specific contact interface. We showed that introducing glycine-to-leucine mutations disrupted PTPRJ oligomerization in cells, promoted PTPRJ association with EGFR, decreased EGFR phosphorylation at tyrosines 1068 and 1173, and antagonized EGFR-driven cell phenotypes. Schwarz et al. observed similar results toward the oncogenic mutant FLT3 (with internal tandem duplications) in acute myeloid leukemia cell models (Schwarz et al., 2022). These results suggest that disrupting the oligomerization of PTPRJ could prove a valuable therapeutic strategy to restrict oncogenic RTK activity in cancer cells.

In response to the lack of specific agonists, we also reported the screening and identification of a transmembrane peptide (RJ_{binder}) that interacts with the TM domain of PTPRJ and disrupts its TM domain-mediated dimerization (Bloch et al., 2019). Treatment of EGFR-driven cancer cells with this peptide resulted in decreased PTPRJ self-association, reduced EGFR phosphorylation, and ultimately inhibited cell migration. This peptide represents a first-in-class agonist and possibly a new allosteric approach to target the activity of RPTPs. However, like for other TM peptides, poor solubility in aqueous solution, need for a delivery vehicle (i.e., detergent micelles), lack of insertion directionality, and indiscriminate insertion in healthy and cancer cells limit its efficacy and applications.

Here, to circumvent these hurdles and improve targeting and efficacy against cancer cells (where RTKs are dysregulated), we combined the properties of the RJ_{binder} with those of the pH (Low) Insertion Peptides (pHLIP), a family of peptides with validated selective tumor targeting and promising therapeutic potential. The pHLIP peptides insert into the plasma membrane of cancer cells in a pH-dependent manner (Burns et al., 2015; Burns et al., 2016; Burns et al., 2017; Burns & Thévenin, 2015; Gerhart et al., 2018) by taking advantage of the inherent acidic microenvironment of solid tumors (Bhujwalla et al., 2002; Gerweck & Seetharaman, 1996; Vaupel et al., 1989; Warburg, 1956; Wike-Hooley et al., 1984; Zhang et al., 2010). We threaded the residues shown to provide pHLIP with aqueous solubility and pH-sensitive insertion into the sequence of RJ_{binder} to engineer hybrid peptides. By making minimal sequence modifications, we show that the resulting lead hybrid peptide (**hybrid7**) is readily soluble in aqueous solution and inserts into membranes as a TM α-helix in a pH-dependent manner without affecting its ability to interfere with PTPRJ oligomerization. Treating cancer cells with **hybrid7** resulted in decreased EGFR phosphorylation, attenuation of downstream signaling, and inhibition of cancer cell migration and proliferation, significantly improving the original, non-pH-sensitive RJ_{binder} peptide.

2 | RESULTS

2.1 | Hybrid peptide design and synthesis

We considered several factors to thread residues conferring pHLIP-like properties into the sequence of RJbinder without affecting its properties. First, we only kept the

TABLE 1 The sequence of the original RJbinder and relevant pHLIP variants.

Name	Sequence	pK_{50}
RJbinder	KKTTLLLLSSIGAIMWVSLVCLIAVKGSNKK	N/A
pHLIP(WT)	GGEQNPIYWARYDWLFTTPLLLLDLALLVDADEGTG	6.16[a]
pHLIP(D14E)	GGEQNPIYWARYEWLFTTPLLLLDLALLVDADEGTG	6.14[a]
pHLIP(D25E)	GGEQNPIYWARYDWLFTTPLLLLELALLVDADEGTG	6.27[a]
pHLIP(D14Aad)	GGEQNPIYWARYAadWLFTTGLLLLDLALLVDADEGTG	6.37[a]
pHLIP(D25Aad)	GGEQNPIYWARYDWLFTTGLLLLAadLALLVDADEGTG	6.74[a]
pHLIP(P20G)	AAEQNPIYWARYDWLFTTGLLLLDLALLVDADEGG	7.2[b]
pHLIP(WT-Ala)	AAEQNPIYWARYDWLFTTPLLLLDLALLVDADEGG	6.1[b]
Hybrid 1	DDDDDDTTLLLLSDIGAIMWVSLVDLIADADEG	This study
Hybrid 2	DDDDDDTTLLLLSDIGAPMWVSLVDLIADADEG	This study
Hybrid 3	DDDDDDTTLLLLSDIGAPMWVSLVELIADADEG	This study
Hybrid 4	DDDDDDTTLLLLSDIGAGMWVSLVELIADADEG	This study
Hybrid 5	DDDDTTLLLLSDIGAGMWVSLVELIADADEG	This study
Hybrid 6	DDDDTTLLLLSDIGAGMWVSLVAadLIADADEG	This study
Hybrid 7	DDTTLLLLSEIGAGMWVSLVELIADADEG	This study
Hybrid 7-control	DDTTLLLLSEIGLGMWVSLVELIADADEG	This study
Hybrid 8	DDTTLLLLSEIGAGMWVSLVELIAEAEEG	This study
Hybrid 9	DDTTLLLLSAadIGAGMWVSLVELIADADEG	This study

[a]Onyango et al. (2015).
[b]Vasquez-Montes et al. (2018).

region of RJ_{binder} predicted to be the TM domain (LLLLSSIGAIMWVSLVCLIA; bold in Table 1). Second, we held the residues S9, A13, and V17 of RJ_{binder} (Table 1; underline residues) constant. We previously identified them as crucial for its activity and likely part of the contact interface with PTPRJ (Bloch et al., 2019). Third, several residues are essential to the pH-responsive properties of pHLIP. For instance, the two aspartic acid residues at positions 14 and 25 (Table 1; red residues) confer pH sensitivity by being protonated at lower pH. Additionally, the proline residue at position 20 (Table 1; green residues) maintains a high energy barrier to membrane insertion until protonation by limiting α-helix formation. Notably, pHLIP insertion properties can be finely tuned by changing these residues to other amino acids. For example, replacing either D14 or D25 with glutamic acid or 2-aminoadipic acid and P20 with glycine increases the pK_{50} (i.e., the pH at which 50% of peptides are in the α-helical membrane inserted state) (Table 1) (Barrera et al., 2012; Musial-Siwek et al., 2010; Onyango et al., 2015; Vasquez-Montes et al., 2018). Fourth, the position and spacing of these residues are also crucial (Fendos et al., 2013) and were conserved in our design while not affecting the residues involved in the interaction of RJ_{binder} with PTPRJ. Finally, given the hydrophobicity of RJ_{binder} and to aid with solubility, insertion unidirectionality, and retention of the inserted state, we included an N-terminal Aspartic tag and the C-terminal region of pHLIP (DADEG) (Barrera et al., 2011; Cunningham & Deber, 2007; Melnyk et al., 2003). With this in mind, we designed and synthesized two hybrid peptides (Table 1; hybrids 1 and 2).

2.2 | Identification of pH-responsive hybrid peptides

To assess whether the hybrid peptides can insert into lipid membranes as TM helices in a pH-dependent manner, we conducted far-UV circular dichroism (CD) and Trp fluorescence spectroscopy measurements with or without large unilamellar lipid vesicles (LUVs) consisting of palmitoyl-2-oleoyl-sn-glycero-3-phosphocholine (POPC) as a function of pH. We selected POPC because it allows comparison with the many reported biophysical measurements with pHLIP and other TM peptides (Alves et al., 2018; Nguyen et al., 2015; Vasquez-Montes et al., 2019; Vasquez-Montes et al., 2022). As observed by CD spectroscopy (Figure S1a), **hybrid1** adopts a mostly disordered conformation at pH 8.0 with and without vesicles and exhibits a slight increase in helical content at pH 4.0 in the presence of vesicles. However,

no change in Trp fluorescence emission is observed in either condition (Figure S1b). With emission maxima centered around 360 nm, these results indicate that the Trp resides in an aqueous environment and that **hybrid1** does not partition into the lipid bilayer. On the other hand, **hybrid2** exhibits spectroscopic signatures consistent with a pH-responsive insertion (Figure 1a,b). As observed by CD spectroscopy (Figure 1a), it adopts a mostly disordered conformation at pH 8.0 in the absence and presence of LUVs and shows an increase in helical content at pH 4.0 with vesicles (74% helical). In the presence of LUVs, **hybrid2** exhibits a blue shift in the Trp emission spectrum from 362 nm at pH 8.0 to 341 nm at pH 4.0 (Figure 1b), indicating a transition of the Trp from a polar, aqueous environment to a more hydrophobic environment such as the lipid bilayer. From analyzing the complete pH titration from 3.0 to 8.0 and the corresponding positions of maxima, we determined a protonation-dependent membrane insertion pK_{50} of 4.8 (Figure 1c and Table 1). While these results are consistent with the desired behavior (forming a TM α-helix upon acidification), we considered a pK_{50} of 4.8 too low for possible future applications.

Therefore, to increase the pK_{50} of insertion, we designed hybrids 3–9 with sequence modifications guided by those established in pHLIP variants (Table 1). All seven peptides exhibited, albeit to a different extent, CD (Figure S2) and Trp fluorescence (Figure S3) spectroscopic signatures similar to **hybrid2** and consistent with a transition of disordered peptides at pH 8 to inserted α-helices upon acidification. They all show a sigmoidal pH response in the presence of vesicles (Figure S4) with pK_{50} from 4.7 to 5.7 (Table S1). Notably, **hybrid7** displayed the highest helical content (Table S1) at low pH in the presence of vesicles (97%) (Figure 2a), the largest blue shift (from 363 to 333 nm) (Figure 2b), and the highest pK_{50} value (5.68) (Figure 2c).

To determine the orientation **hybrid7** adopts in the presence of vesicles at lower pH, we performed oriented circular dichroism (OCD), which allows for the differentiation between transmembrane and interfacial α-helices (Bürck et al., 2016; Wu et al., 1990). OCD measurements at low pH in the presence of POPC vesicles yielded a spectrum with a single minimum of around 230 nm (Figure 2d; red line), consistent with an inserted TM helix. On the other hand, the OCD spectrum at pH 8.0 has a single minimum at ~210 nm (Figure 2d; blue line), which is not consistent with either a TM or interfacial α-helix but is consistent with an unstructured peptide and the CD results (Figure 2a). Given its favorable properties, we selected **hybrid7** as the lead peptide for further evaluation.

2.3 | Hybrid7 associates with the transmembrane domain of PTPRJ

To assess whether the sequence modifications made to obtain **hybrid7** affect the ability of the peptide to interfere with PTPRJ dimerization, we used the dominant-negative AraC-based transcriptional reporter assay (DN-AraTM) (Barton et al., 2015; Deng et al., 2014; Goh et al., 2018; Su & Berger, 2012; Su & Berger, 2013; Wonganu & Berger, 2016). This assay reports on the propensity of TM domains to self-associate and heterodimerize in cell membranes and allowed us, in a previous study, to identify the disruptive glycine-to-leucine TM mutations and the RJ_{binder} peptide (Bloch et al., 2019). Briefly, the assay relies on a protein chimera containing the receptor domain of interest fused to either the transcription factor AraC (which is active at the

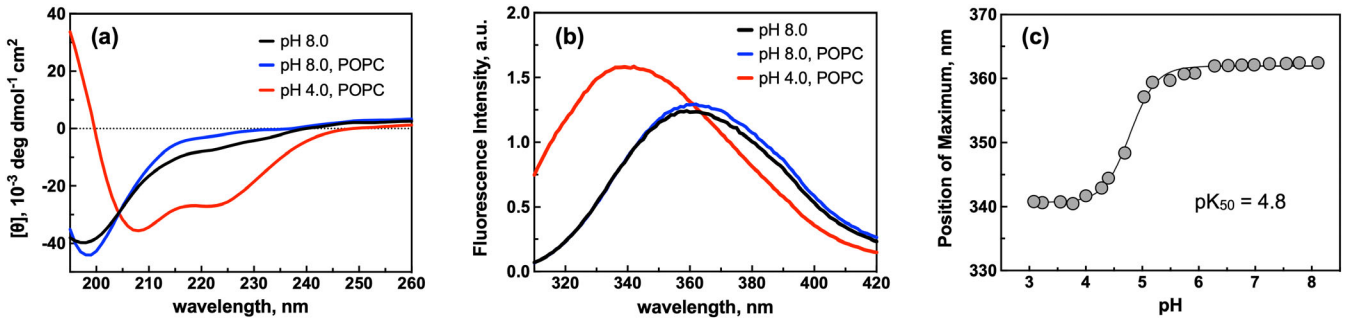

FIGURE 1 Hybrid2 inserts into the membrane of lipid vesicles in a pH-dependent manner. The interaction of hybrid2 with lipid membranes was assessed by (a) circular dichroism and (b) Trp fluorescence in the absence (black) or presence of large unilamellar POPC lipid vesicles at pH 7.4 (blue) and pH 4.0 (red). (c) Determination of the pH midpoint (pK_{50}) for the insertion of hybrid2 into POPC vesicles monitored by determination of the Trp fluorescence emission maximum as a function of pH.

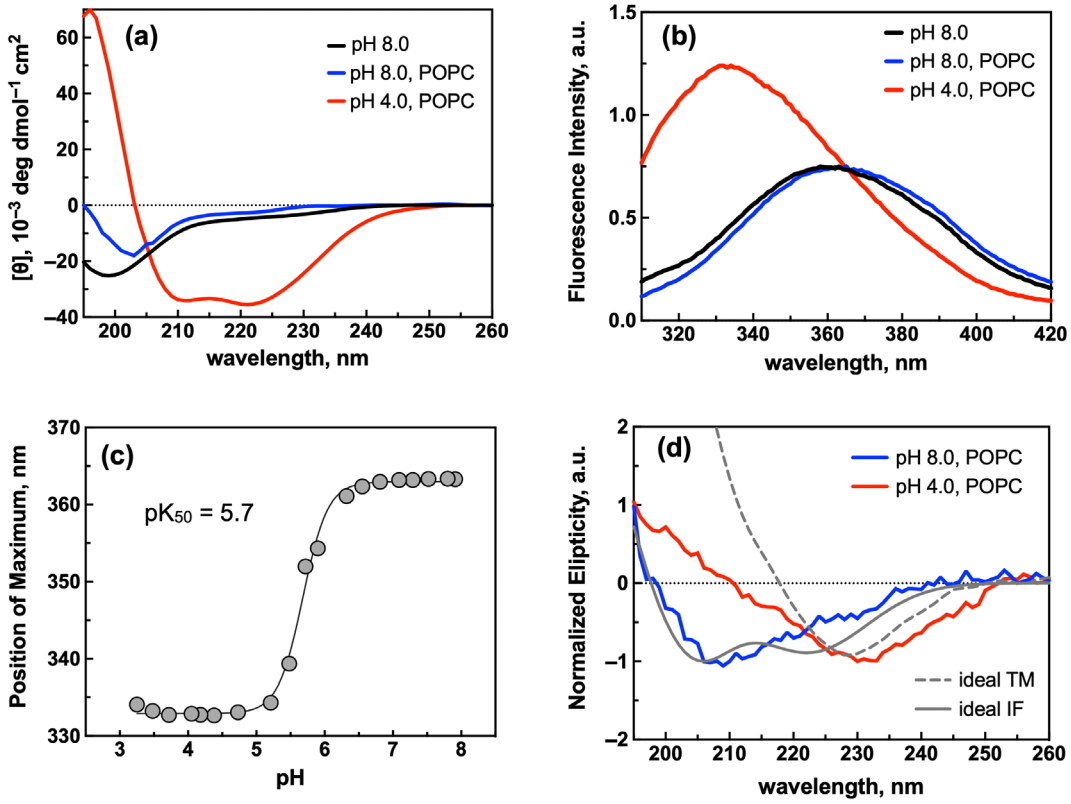

FIGURE 2 Hybrid7 inserts into the membrane of lipid vesicles in a pH-dependent manner. The interaction of hybrid =7 with lipid membranes was assessed by (a) circular dichroism and (b) Trp fluorescence in the absence (black) or presence of large unilamellar POPC lipid vesicles at pH 7.4 (blue) and pH 4.0 (red). (c) Determination of the pH midpoint (pK_50) for the insertion of hybrid7 into POPC vesicles by determination of the Trp fluorescence emission maximum as a function of pH. (d) Oriented circular dichroism spectra of hybrid7 at low pH or in the presence of POPC vesicles. The theoretical spectra for ideal transmembrane (0°) and interfacial (90°) helices are shown for comparison.

ara*BAD* promoter as a homodimer) or an AraC mutant unable to activate transcription (AraC*). Homodimerization of AraC (a result of receptor domain self-association) induces the transcription of the gene coding for the green fluorescent protein (GFP). On the other hand, preferential TM-mediated AraC-AraC* heterodimerization reduces the level of GFP transcription. Thus, the level of GFP fluorescence intensity is a measure of receptor domain homo- or hetero-dimerization.

Figure 3 shows that **hybrid7** retains the ability to interact with the TM of PTPRJ. Indeed, the co-expression of **hybrid7** as a competitor to PTPRJ-AraC led to a significant decrease in GFP expression (Figure 3; 1 vs. 3), indicative of a preferential heterodimer. This decrease is comparable to the one observed when the TM sequence of PTPRJ is co-expressed as a competitor (Figure 3; 1 vs. 2). As a control, we also tested the effect of mutating A13 to leucine in **hybrid7**. We previously showed that A13L causes RJ_{binder} to lose its ability to out-compete PTPRJ oligomerization by interfering with helix-packing (Bloch et al., 2019). Similarly, the point mutation significantly hampers **hybrid7** efficacy to interact with PTPRJ (Figure 3; 1 vs. 4), even though it exhibits an increased expression (Figure S6a). Noteworthy, neither **hybrid7** nor **hybrid7-control** sequences show a propensity to dimerize (Figure S6b): Both show a low signal compared to the strongly interacting transmembrane domain of the leukocyte receptor tyrosine kinase (LTK) (Finger et al., 2009) when the AraC fusions are expressed alone (Figure S6b; 1 vs. 4 and 1 vs. 7). Co-expression of the AraC* fusion does not decrease that signal significantly either (Figure S6b; 4 vs. 5 and 7 vs. 8), indicating that there is no competition between the two fusions. Hybrid7 not having the propensity to self-interact is an advantageous property because its oligomerization would likely hinder its interaction with PTPRJ. A peptide corresponding to the A13L variant was synthesized and subsequently used as a negative control peptide (**hybrid7-control**). Moreover, the A13L substitution did not significantly affect the ability of **hybrid7-control** to form a pH-inducible TM α-helix or the pK_{50} of insertion (Table S1 and Figure S5).

To better understand the molecular interactions between **hybrid7** and the TM domain of PTPRJ, we also

performed 70 ns replica exchange molecular dynamics (REMD), followed by 1 μs all-atom MD simulations in the POPC bilayer (Figure 4b and Figure S7). The resulting model shows a left-handed heterodimer with a crossing angle of +19 degrees that positions the acidic residues away from the contact interface (Figure 4a). The inter-TM contact probability map (Figure 4b and Figure S7c) shows contact mainly through residues Leu5, Leu 8, Gly12, Leu19, and Leu22 on **hybrid7**, and Phe12, Phe16, Leu19, Thr23, and Trp30 on PTPRJ. It suggests that PTPRJ interacts with **hybrid7** through different residues than those we identified to mediate its homodimerization (Gly9, Gly13, and Gly17). It also indicates that, while Ala13 on **hybrid7** does not have the highest probability of inter-TM contact, it is still a 'hot spot' for interaction with PTPRJ (Figure 4b and Figure S7c). It is also the case for Ser9, whose substitution for leucine disrupts PTPRJ TM-TM interaction (Bloch et al., 2019). This is consistent with the results obtained with the DN-AraTM reporter assay and the influence of A13 on **hybrid7** interaction with PTPRJ. However, we recognize the differences between the results from MD simulations and experimental observations. A more in-depth understanding of the contact interfaces is the focus of ongoing work.

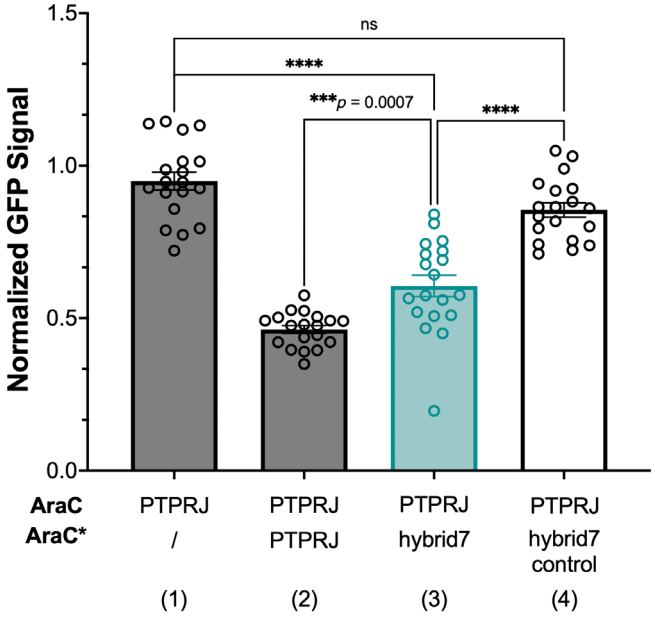

FIGURE 3 Assessing the interaction of hybrid7 with PTPRJ. Quantifying the disruption of PTPRJ oligomerization by hybrid7 using the DN-AraTM assay. The GFP signal is normalized to the signal of PTPRJ homodimer (1), and the results are shown as mean ± S.E. ($n = 18$). Bacteria are always transformed with both AraC* and AraC-containing plasmids. The slash (/) represents the empty AraC* vector without the TM construct of interest. The level of significance (one-way ANOVA with Tukey's multiple comparisons correction, p value <0.05) is shown. ****, $p < 0.0001$; ns, $p > 0.05$.

2.4 | Hybrid7 inserts into cancer cell membranes without disruption

To assess the interaction of **hybrid7** with cells, we treated HSC3 cells (an EGFR-driven human squamous cell carcinoma line we previously engineered to express full-length PTPRJ (Bloch et al., 2019)) with **hybrid7** labeled

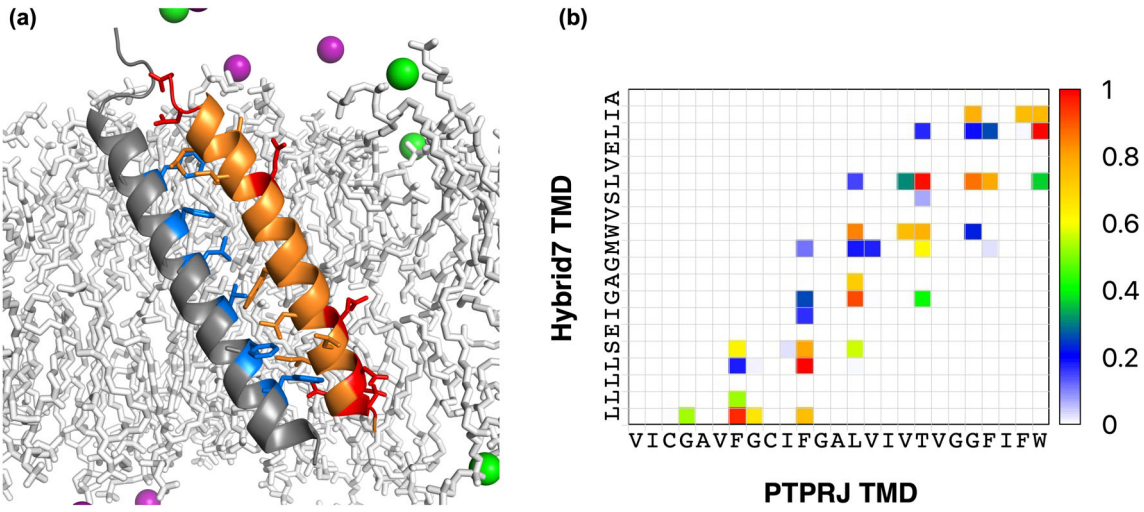

FIGURE 4 Structure models of PTPRJ-Hybrid7 heterodimer in explicit POPC lipid bilayer from MD simulations. (a) Representative snapshot of the PTPRJ-Hybrid7 heterodimer model equilibrated in a fully atomistic POPC bilayers from five 1 μs simulations. PTPRJ and hybrid7 are shown in gray and orange, respectively. Aspartic and glutamic acids in hybrid7 are shown in red, residues on PTPRJ at the contact interface are shown in blue, and POPC is shown in white. Potassium and chloride ions are shown in green and purple, respectively. Water, hydrogen, and components in front of the PTPRJ-Hybrid7 assembly are omitted for clarity. (b) Inter-TM contact probability of PTPRJ-Hybrid7 heterodimer model from MD simulations. Data were averaged over five 800-ns trajectories.

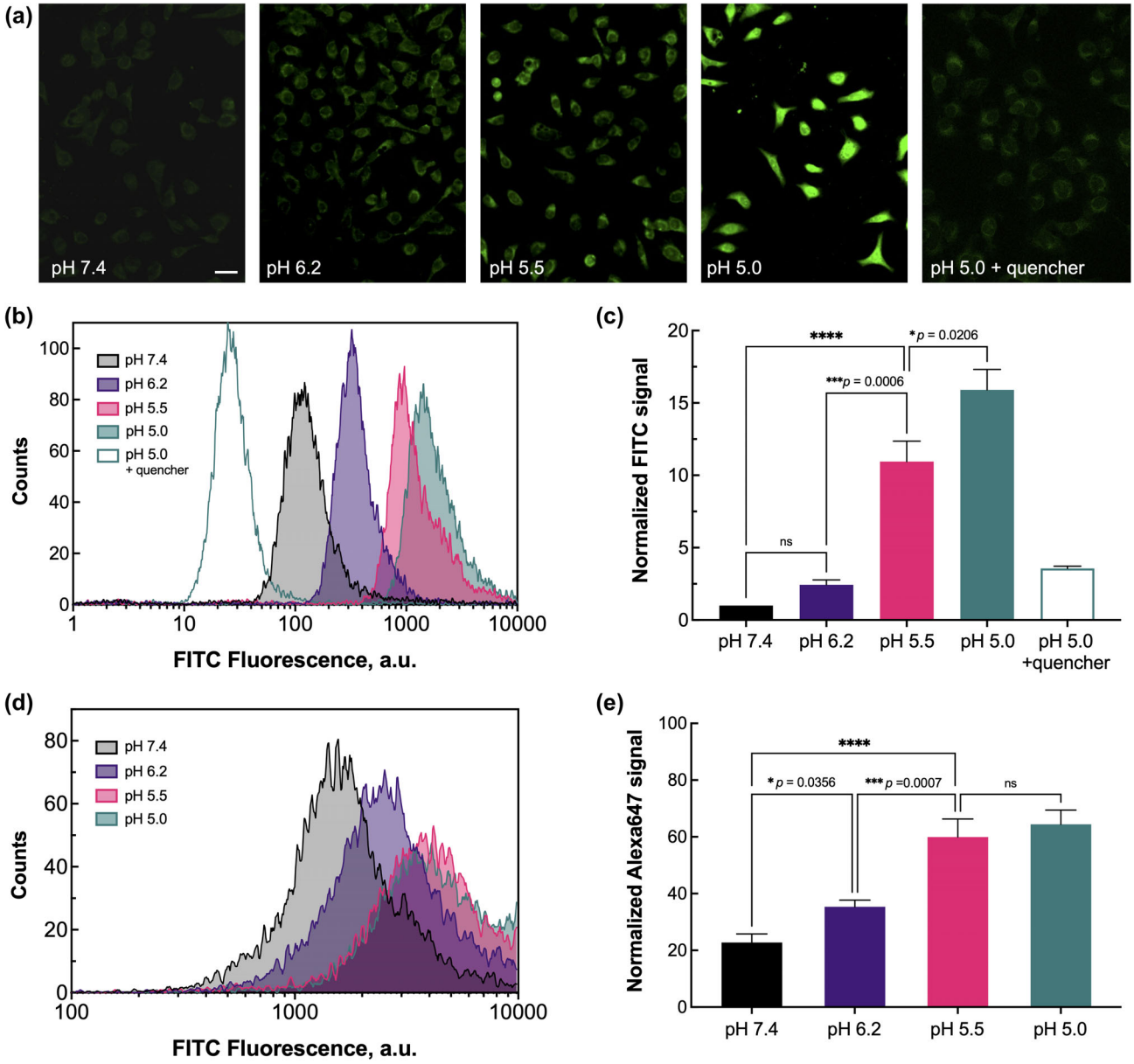

FIGURE 5 Hybrid7 inserts into the membrane of cells in a pH-dependent manner. The insertion of FITC-hybrid7 in cell membranes was assessed by fluorescence microscopy (a) and quantified by flow cytometry (b and c). HSC3 cells were treated with 5 μM of FITC-hybrid7 for 10 min at the indicated pH. After washing and fixing (and quenching by trypan blue after treatment at pH 5.0), cells were imaged by fluorescence microscopy. Scale bar, 200 μm. The relative amount of fluorescence was also quantified by flow cytometry. (b) Representative examples of flow cytometry histograms. (c) Summary of the flow cytometry data. The insertion topology of FITC-hybrid7 was assessed by the recruitment of Alexa647-labeled anti-FITC antibodies at the surface of HSC3 cells. (d and e) The amount of antibody recruitment was quantified by flow cytometry. (d) Representative examples of flow cytometry data are shown. (e) Summary of the flow cytometry data. Results are shown as mean ± S.E. ($n = 3$–6). The level of significance (one-way ANOVA with Tukey's multiple comparisons correction, p value <0.05) is shown. ****, $p < 0.0001$; ns, $p > 0.05$. Only a subset of comparisons is shown for clarity.

at its N-terminus with fluorescein (FITC-hybrid7). Labeling **hybrid7** with FITC does not significantly alter its pH-responsive structure, insertion, and pK_{50} (6.0 vs. 5.7 for **hybrid7**) (Table S1 and Figure S5).

While **FITC-hybrid7** showed minor interactions with cells at physiological pH 7.4, progressive acidification resulted in an increase of FITC fluorescence intensity (Figure 5a), attributed to the pH-dependent membrane insertion of **hybrid7**. We also quantified this interaction by flow cytometry. Consistent with what was observed qualitatively by microscopy, the relative amount of **FITC-hybrid7** detected on the cells increased in a pH-

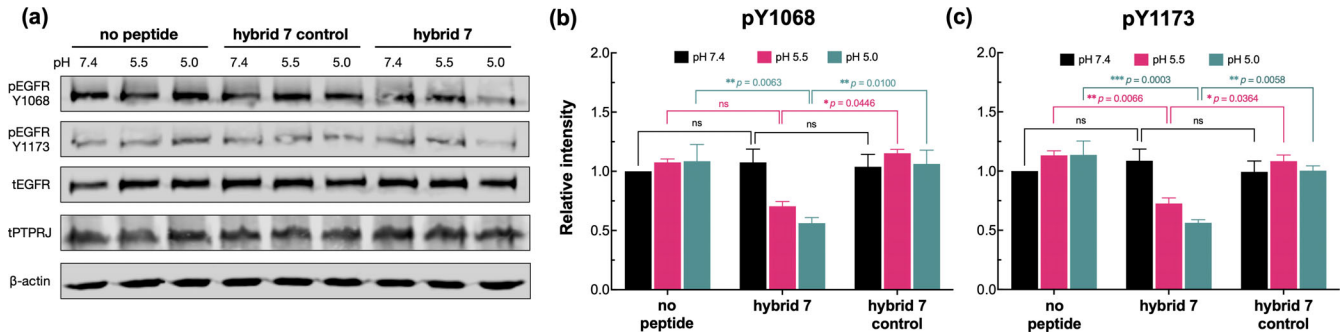

FIGURE 6 Hybrid7 inhibits the phosphorylation of EGFR. Serum-starved HSC3 cells ectopically expressing PTPRJ were treated with 10 μM of hybrid7 or hybrid7-control for 10 min at the indicated pHs before stimulation with EGF. Cell lysates were probed for EGFR, phospho-EGFR (Tyr-1068 and Tyr-1173), and PTPRJ by immunoblotting. (a) Representative blots from the same samples are shown. (b, c) The relative (ratio of phosphorylated to total protein) intensities are shown as mean ± S.E. ($n = 4$–6). The level of significance (one-way ANOVA with Tukey's multiple comparisons correction, p value <0.05) is shown. ****, $p < 0.0001$; ns, $p > 0.05$. ns, $p > 0.05$. Only a subset of comparisons is shown for clarity.

dependent manner, with a 12-fold (pH 5.5) and 16-fold (pH 5.0) increase in fluorescence over that at pH 7.4 (Figure 5b,c). Moreover, in both microscopy and flow cytometry experiments, FITC fluorescence is quenched by the extracellular addition of trypan blue (a known quencher of fluorescein emission (Cowen et al., 1985; Hed et al., 1987; Van Amersfoort & Van Strijp, 1994)) (Figure 5b,c), indicating that FITC (and therefore the N-terminal end of hybrid7) is extracellularly exposed. Finally, the exposure of FITC to the extracellular environment was confirmed by flow cytometry, showing an increase in the recruitment of anti-FITC antibodies upon a decrease in pH (Figure 5d,e). This result is consistent with what we observed in another study using pHLIP labeled at its N-terminus with FITC (Wehr et al., 2020).

With confirmation that **hybrid7** selectively associates with cell membranes in a pH-responsive manner, we sought to determine whether the insertion damages the integrity of the lipid bilayer. Following a 1-h treatment with 10 μM of **hybrid7** at pH 7.4, 5.5, or 5.0, the media from the HSC3 cells was analyzed for the release of the intracellular enzyme lactate dehydrogenase (LDH), a proxy for membrane integrity. Neither **hybrid7** nor low pH treatment causes a significant release of LDH (Figure S7), indicating that the peptide does not cause membrane disruption, consistent with our previous results obtained with pHLIP (Burns et al., 2015; Burns et al., 2016; Burns et al., 2017; Burns & Thévenin, 2015).

Altogether, these results indicate that **hybrid7** inserts in the plasma cell membrane in a pH-dependent manner with its N-terminal end remaining extracellularly (like pHLIP) without disrupting the cell plasma membrane.

2.5 | Hybrid7 inhibits EGFR phosphorylation, EGFR-Driven cell migration, and proliferation in a pH-dependent manner

Next, we determined the functional effect of **hybrid7** on the activity of PTPRJ in cells. We hypothesized that treating cells with **hybrid7** at lower pH would decrease EGFR signaling and, ultimately, inhibit EGFR-driven cell migration and proliferation while having no effect at higher pH.

Figure 6 shows that 10 min treatment of HSC3 cells expressing wild-type PTPRJ with 10 μM **hybrid7** resulted in a significant pH-dependent decrease in EGFR phosphorylation at both Tyr-1068 and Tyr-1173 (30% and 45% reduction at pH 5.5 and pH 5.0, respectively). On the other hand, no changes in phosphorylation level were observed after treatment with **hybrid7-control**.

Additionally, results in Figure 7 show that similar treatment with **hybrid7** inhibits EGFR-driven cell migration in a pH-dependent manner. At pH 7.4 and 5.5, **hybrid7** had no significant effect on cell migration but decreased cell migration by 60% at pH 5.0. While treatment with **hybrid7-control** does not result in any effect at pH 5.5, a 30% inhibition in cell migration was observed when cells were treated at pH 5.0.

Lastly, **hybrid7** inhibits cell proliferation in a concentration and pH-dependent manner (Figure 8a). At pH 7.4, **hybrid7** had minimal effect on cell viability, with a maximum decrease of 30% at 10 μM. On the other hand, a significant concentration-dependent decrease in cell viability was observed at pH 5.5, with only 20% viability at 10 μM and an IC_{50} of 0.54 μM. Noteworthy, **hybrid7-control** had no effect at either high or acidic pH (Figure 8b), and **hybrid7** did not affect the parental

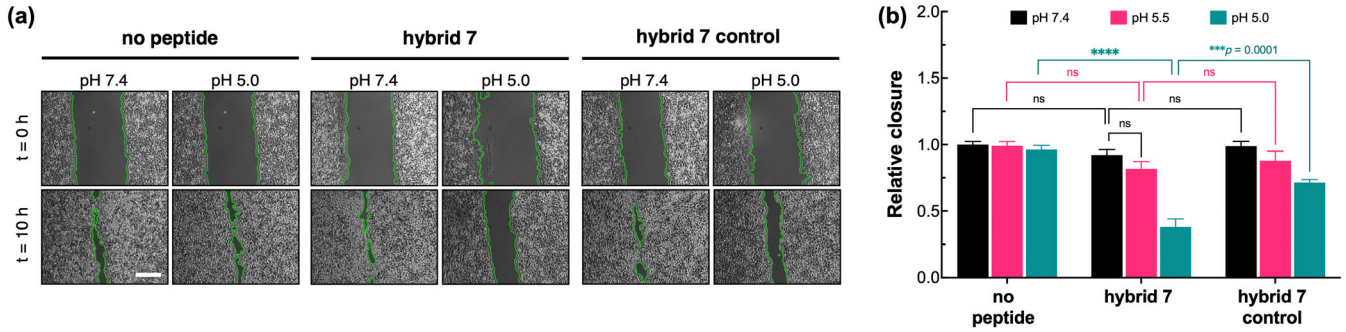

FIGURE 7 Hybrid7 inhibits EGFR-driven cell migration. Representative phase-contrast images with tracings to identify open scratch areas (a) and quantification (b) of the effect of hybrid7 and hybrid7-control on wound closure. Serum-starved HSC3 cells ectopically expressing PTPRJ were treated with 10 μM of peptide for 10 min at the indicated pH, scratched (0 h), and incubated in complete medium with EGF (50 ng/mL) for 10 h. Relative closure was quantified by calculating the percentage change in the area between 0 and 10 h using ImageJ and then normalized to medium containing EGF. Scale bar, 300 μm. (b) Summary of the wound healing data. Results are shown as mean ± S.E. ($n = 8$–11). The level of significance (one-way ANOVA with Tukey's multiple comparisons correction, p value <0.05) is shown. ****, $p < 0.0001$; ns, $p > 0.05$. Only a subset of comparisons is shown for clarity.

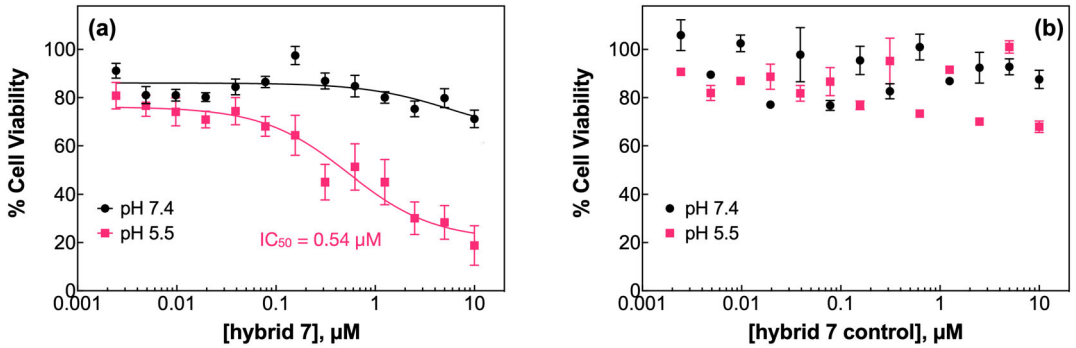

FIGURE 8 Hybrid 7 inhibits cell proliferation in a pH- and concentration-dependent manner. HSC3 cells expressing PTPRJ ectopically were incubated with (a) hybrid7 or (b) hybrid7-control at pH 7.4 or 5.5 for 10 min, washed, and recovered for 72 h in complete media. Cell viability was assessed by MTT assay. All measurements are normalized to cells treated at pH 7.4 only (100% viability). Results are shown as mean ± S.E. ($n = 9$). When possible, data were fitted to a sigmoidal dose response.

HSC3 cells expressing a minimal level (undetectable by immunoblot) of PTPRJ (Figure S8) (Bloch et al., 2019). Crucially, cell treatment at lower pH did not affect either EGFR phosphorylation (Figure 6), cell migration (Figure 7) or proliferation (Figure 8).

Taken together, our results strongly indicate that **hybrid7** disrupts, in a pH-dependent manner, the TM domain-mediated dimerization of PTPRJ, thereby enhancing PTPRJ's ability to dephosphorylate EGFR and attenuating downstream signaling cascades and EGFR-driven phenotypes.

3 | DISCUSSION

Because of the lack of clear agonists for PTPRJ and its tumor-suppressor role, promoting its activity toward EGFR and other substrate RTKs represents a much-needed and unique way to study PTPRJ signaling mechanisms and a promising therapeutic modality in oncology. In this work, we engineered an allosteric agonist of PTPRJ, **hybrid7**, that is readily soluble in aqueous buffer and inserts as a helical TM domain into cell membranes without disrupting them under acidic conditions that resemble the microenvironment of tumors.

Our results also support that **hybrid7** interacts with PTPRJ and promote its activity toward EGFR, leading to reduced EGFR phosphorylation and inhibition of EGFR-driven cell migration and proliferation. **Hybrid7** disrupts these processes more efficiently than the previously reported G-to-L TM point mutations and the RJ_{binder} peptide. For example, treatment with RJ_{binder} at the same concentration (10 μM) decreased phosphorylation at Tyr-1068 and Tyr-117 by only ~20%–30% (45% reduction for **hybrid7** at pH 5.0) and cell migration by 20% (vs. 60% reduction for **hybrid7** at pH 5.0) (Bloch et al., 2019). RJ_{binder} also required 1-h treatment to achieve these results, while cells were only treated with hybrid7 for

10 min. **Hybrid7** also inhibits cell proliferation with a promising IC50 of 0.5 μM.

Although our results indicate that the TM Glu residues are not part of the contact interface between **hybrid7** and PTPRJ, acidic residues may provide additional specificity to TM interactions (Bañó-Polo et al., 2013; Gratkowski et al., 2001; Zhou et al., 2001). The addition of these residues may afford **hybrid7** additional efficacy and could explain some of the small effects **hybrid7-control** had on pEGFR and cell migration. Moreover, it is likely that the single point mutation in **hybrid7-control** hinders the ability to interact with PTPRJ but does not entirely abrogate it. Based on our MD simulation results, the residues neighboring Ala13 (mutated to a Leu in **hybrid7-control**) may also contribute to the association with PTPRJ. It is also possible that the presence of PTPRJ in the cell membrane may favor the inserted state, raising the apparent pK_{50} of insertion. It could also explain the observed efficacy of **hybrid7** in cells even at a pH relatively far from its determined pK_{50} in vesicles. This was observed with the TYPE7 peptide designed to bind to the TM of EphA2 in a pH-dependent manner, for which the presence of EphA2 in vesicles increased the pK_{50} from 6.18 to 6.85 (Alves et al., 2018). However, based on this result, the efficacy of TYPE7 in cells was only tested at normal physiological pH, making it impossible to assess its pH-mediated selectivity. Nevertheless, improving the efficacy of **hybrid7** by tuning its pH_{50} of insertion and its contact interface with PTPRJ is the focus of ongoing efforts in our laboratory.

In conclusion, **hybrid7** represents a first-in-class tumor-targeting allosteric agonist of RPTPs, and we expect that the basic framework developed here can be extended to other RPTPs (and, therefore, other RTK substrates). Indeed, modulation of RPTP activity through dimerization of TM domains is a general theme throughout the family, and targeting the TM domains could, therefore, offer a level of specificity that cannot be achieved by targeting either the extracellular or PTP domains alone. While this strategy is therapeutically relevant to tumors driven by oncogenic RTK signaling, it also presents an alternative approach for RPTP activation to study their function and identify new substrates in cells.

4 | EXPERIMENTAL SECTION

4.1 | Solid-phase peptide synthesis

Hybrid peptides were prepared by solid-phase peptide synthesis, purified and analyzed by RP-HPLC, and confirmed via MALDI-TOF mass spectrometry, as previously reported (Bloch et al., 2019; Gerhart et al., 2018; Vasquez-Montes et al., 2019; Vasquez-Montes et al., 2022; Wehr et al., 2020).

4.2 | Sample preparation of hybrid peptides for circular dichroism (CD) and tryptophan fluorescence measurements

All peptides were first solubilized to 20 μM in 5 mM sodium phosphate (pH 8.0). Each peptide was diluted to a final concentration of 7 μM before analysis. 100 nm 1-palmitoyl-2-oleoyl-sn-glycero-3-phosphocholine (POPC) large unilamellar vesicles were prepared by freeze–thaw and extrusion, as previously reported (Bloch et al., 2019; Gerhart et al., 2018; Vasquez-Montes et al., 2019; Vasquez-Montes et al., 2022; Wehr et al., 2020). Peptides were incubated with the resulting vesicles at a 1:300 ratio. The pH was adjusted to the desired experimental values with HCl, and the samples were incubated for 30 min at room temperature prior to spectroscopic analysis.

4.3 | CD spectroscopy

Far-UV CD spectra were recorded on a Jasco J-815 CD spectrometer equipped with a Peltier thermal-controlled cuvette holder (Jasco). Measurements were performed in a 0.1 cm quartz cuvette. Raw data were acquired from 260 to 190 nm at 1 nm intervals with a 100 nm/min scan rate, and at least five scans were averaged for each sample. The spectrum of POPC liposomes was subtracted from all construct samples. CD intensities are expressed in mean residue molar ellipticity [θ] calculated from the following equation:

$$[\theta] = \theta_{obs}/10.l.c.n\left(\text{in}\,deg.cm^{-2}.dmol^{-1}\right),$$

where θ_{obs} is the observed ellipticity in degrees, l is the optical path length in centimeters, c is the final molar concentration of the peptides, and n is the number of amino acid residues. Percent helical folding was calculated assuming ellipticity at 222 nm corresponds only to α-helical content:

$$\%\text{helical content} = \frac{[\theta]_{222}}{[\theta]_{222}^{max}\left(1-\frac{k}{n}\right)} \times 100,$$

where $[\theta]_{222}$ is the observed ellipticity at 222 nm, $[\theta]_{222}{}^{Max}$ is the theoretical mean residue ellipticity for an infinitely long helical peptide (−39,500 deg·cm [Manning et al., 2002]·$dmol^{-1}$), n is the number of residues, and k is a wavelength-dependent constant (2.57 at 222 nm) (Chen et al., 1974).

4.4 | Oriented circular dichroism (OCD)

OCD measurements were performed using a JASCO-810 spectropolarimeter (JASCO, Easton, MD). Spectra were obtained by creating a stack of oriented multilayers on a quartz disc as previously described (Vasquez-Montes et al., 2019; Vasquez-Montes et al., 2022; Wimley & White, 2000). Briefly, 0.1 mM hybrid7 and a 10 mM POPC were co-dissolved in methanol (1:100 peptide to lipid ratio). The multilayer stack was created by placing 2.5 μ l of the peptide/lipid mixture in the center of a 2.5 cm disc. The solvent was then air-dried to a 1 cm diameter and hydrated using warm air at ~100% relative humidity. A drop of 5 mM HEPES buffer pH 4 or 5 mM HEPES buffer pH 8 was added between each stack layer and completely dried before continuing with multilayer stacking. The disc containing the multilayer stack was mounted on a sealed tube with the sample side pointing inwards. An average of 50 scans was collected at eight different orientations at 45 degree intervals along the central axis. The collected spectra were averaged, and the background signal (determined by collecting the spectra of a multilayer stack in the absence of peptide) was subtracted. The presented spectra have been normalized to the ellipticity of their respective minimum due to difficulties calculating the peptide concentration along the beam path of each stack.

4.5 | Tryptophan fluorescence spectroscopy

Fluorescence emission spectra were acquired with a Fluorolog-3 Spectrofluorometer (HORIBA). The excitation wavelength was set at 280 nm, and the emission spectrum was measured from 300 to 450 nm with excitation and emission slits set to 5 nm. The positions of the maximum of the averaged spectra were determined by fitting them to a lognormal distribution using the following formula (Ladokhin et al., 2000) and Origin (Origin Lab):

$$\text{For}\lambda > \lambda_{max} - \frac{\rho\Gamma}{\rho^2-1},$$

$$I(\lambda) = I_0 \exp\left[\frac{ln2}{ln^2\rho} ln^2\left(1+\frac{(\lambda-\lambda_{max})(\rho^2-1)}{\rho\Gamma}\right)\right],$$

$$\text{While for}\lambda < \lambda_{max} - \frac{\rho\Gamma}{\rho^2-1}, I(\lambda) = 0,$$

where I_0 is the maximal intensity of the analyzed spectrum at the fluorescence maximum λ_{max}, Γ is the width of the spectrum at the half maximum intensity, and ρ represents the asymmetry of the distribution.

4.6 | Determining pK_{50} of hybrid peptides

Hybrid peptides (7 μM) were prepared in the presence of LUVs at pH 8.0, as described above. Successive changes of ~0.2 pH units were achieved by adding small volumes of HCl. After each titration, the tryptophan emission spectra were measured, and the positions of the maximum emission were determined as above. The pK_{50} of the insertion for each hybrid peptide was calculated by fitting the fluorescence emission data to the following equation using nonlinear least-square analysis (Fendos et al., 2013; Kyrychenko et al., 2015):

$$\lambda = \frac{\lambda_H + \lambda_L\left(10^{m(pK_{50}-pH)}\right)}{1+10^{m(pK_{50}-pH)}},$$

where λ is the Trp position of maximum measured as a function of pH, the λ_H and λ_L parameters correspond to the saturating Trp positions of maximum at high and low pH, *m* is the transition slope, and pK_{50} denotes the negative logarithm of the dissociation constant.

4.7 | Computational methods

4.7.1 | PTPRJ-hybrid7 heterodimer assembly in implicit bilayer

To model the PTPRJ-hybrid7 heterodimer, we employed replica exchange molecular dynamics (REMD) simulations (Sugita & Okamoto, 1999). The sequences of PTPRJ and hybrid7 used are given below, and the TM domains are underlined. Considering the low pH environment, aspartic and glutamic acids (marked in bold) were all protonated.

PTPRJ Acetyl-^{1}PQ**D**PGVICGAVFGCIFGALVIVTVGGFIFWRKKRK$_{35}$-CONH$_2$.

Hybrid7 NH$_3$-^{1}**DD**TTLLLLS**E**IGAGMWVSLV**E**LIA-**DADE**G^{29}-CONH$_2$.

The initial configuration of the PTPRJ-hybrid7 heterodimer for each replica was prepared as follows. The principal axes of PTPRJ and hybrid7 TM helices were aligned to the membrane normal (z-direction), and the C-termini of TM helices were inserted into the cytosolic side. The helices were separated by 30 Å with random orientations (rotations along each principal axis). For 52 replicas in a temperature range of 300–1000 K, a 70-ns

REMD simulation was performed in the GBSW implicit membrane model (Im et al., 2003) using CHARMM (Brooks et al., 2009). The Langevin dynamics simulation was performed with a collision frequency of 5 ps^{-1}, and the integration time step was set to 2 fs with the SHAKE algorithm (Ryckaert et al., 1977) for constraining covalent bonds involving hydrogen atoms. For the implicit membrane, the GBSW default options provided in Implicit Solvent Modeler in CHARMM-GUI (Jo et al., 2008) were used except for an empirical surface tension coefficient (0.03 kcal/mol/Å (Manning et al., 2002)) for the nonpolar solvation contribution. Replica exchanges were attempted every 1 ps, controlled by the CHARMM REPDSTR module (Woodcock et al., 2007). The centroid structure obtained from the cluster analysis (see below) was used to model the initial structures of PTPRJ-Hybrid7 assembly in an explicit bilayer.

4.7.2 | Molecular dynamics simulations in explicit lipid bilayer

The stability of the obtained structure model (centroid) of PTPRJ-Hybrid7 heterodimers from REMD simulations was examined by molecular dynamics (MD) simulations of the TM assembly in an explicit POPC bilayer, consisting of the heterodimer, 90 and 89 POPC lipids in the upper and lower leaflets, respectively, and bulk water with 150 mM KCl. The membrane system was prepared using the CHARMM-GUI *Membrane Builder* (Wu et al., 2014), and equilibrated by a series of short constant volume and temperature (NVT) and constant temperature and pressure (NPT) simulations, during which various restraints were gradually relaxed. A 1-μs restraint-free NPT simulation was followed for production. For better statistics, we carried out five independent simulations. All simulations were performed using OpenMM (Eastman et al., 2017; Lee et al., 2016) with the C36 protein (Huang & MacKerell, 2013) and lipid (Klauda et al., 2010) force fields and TIP3P water model (Jorgensen et al., 1983; MacKerell et al., 1998). Integration time steps for equilibration were set to 1 fs and 2 fs for NVT and NPT simulations with SHAKE algorithm (Ryckaert et al., 1977), respectively. For the production run, the integration time step was set to 4 fs with the hydrogen mass repartitioning technique (Gao et al., 2021; Hopkins et al., 2015). The van der Waals interactions were smoothly switched off over 10–12 Å by a force-based switching function (Steinbach & Brooks, 1994), and the electrostatic interactions were calculated by the particle-mesh Ewald method (Essmann et al., 1995). The temperature (T = 303.15 K) and the pressure ($p = 1$ bar) were controlled by Langevin dynamics with a friction coefficient of 1 ps^{-1} and a semi-isotropic Monte Carlo barostat (Åqvist et al., 2004; Chow & Ferguson, 1995) with a pressure coupling frequency of 100 steps, respectively.

4.7.3 | Analysis

The sampled conformations from REMD were evaluated by hierarchical clustering, where initially, all sample conformations were assigned to different clusters. Starting from these initial clusters, two clusters were merged when the average root mean square deviation between Cα atoms (Cα-RMSD) for all inter-cluster conformation pairs was less than a cut-off value of 3 Å. The clustering was iterated until there was no cluster closer than the RMSD cut-off. The clustering was done for seven 10-ns blocks of trajectories from the replica at $T = 300$ K. The centroid of the largest cluster during the last 40 ns was chosen as the structural model of PTPRJ-hybrid7 TM assembly. For TM models in explicit POPC bilayer, we calculated Cα-RMSD from their initial structure and inter-TM contact probability. For a conformation at a given time frame, the contact state between a pair of residues is assigned to 1 when the minimum distance between heavy atoms in the residue pair is smaller than 4.5 Å and 0 otherwise. The last 800-ns trajectories from each replica were analyzed. Also, representative conformations of PTPRJ-hydrid7 TM dimer in a POPC bilayer were obtained from the cluster analysis based on the pairwise Cα-RMSD between conformations with the same cut-off.

4.8 | Cell culture

Engineered human tongue squamous cell carcinoma HSC3 cells previously engineered to express wild-type PTPRJ ectopically (Bloch et al., 2019) were cultured in DMEM high glucose supplemented with 10% FBS, 100 units/mL penicillin, and 0.1 mg/mL streptomycin, in a humidified atmosphere of 5% CO_2 at 37°C.

4.9 | Cell treatment and assessment of EGFR Tyr phosphorylation level

HSC3 cells were seeded in 12-well plates at 80,000 cells/well and incubated overnight. The cell media was replaced with serum-free media for 2 h before peptide treatment. Hybrid7 and hybrid7-control were solubilized in an appropriate amount of serum-starved media, pH 7.4, so that upon pH adjustment, the desired

treatment concentration (10 μM) was obtained. The peptides were added to serum-starved cells and allowed to incubate for 5 min at 37°C. The media was then adjusted to the desired pH using a pre-established volume of serum-free media buffered with citric acid, pH 2.0. After a 10 min incubation at 37°C, the treatment media was removed and replaced with fresh serum-free media containing EGF (10 ng/mL), and the cells were incubated for another 10 min at 37°C. Cells were solubilized by the addition of cell extraction buffer supplemented with broad-spectrum phosphatase and protease inhibitors (Pierce #88667), spun down, and the supernatant was mixed with loading buffer. Samples were boiled for 10 min at 95°C and resolved by SDS-PAGE on an 8% tris-glycine gel. Subsequently, the samples were transferred onto a 0.45 μm nitrocellulose membrane (GE Healthcare #1060002) at 100 V for 1 h at 4°C. Membranes were blocked with 5% bovine serum albumin (BSA) in tris-buffered saline Tween 20 (TBS-T) for 1 h at RT and then blotted for phosphorylated EGFR (pY1068: RRID:AB_2096270; pY1173: RRID:AB_331795). When blotting for total proteins (EGFR:RRID:AB_2246311; β-Actin: RRID:AB_2242334; PTPRJ: RRID:AB_2935775), the membranes were blocked with 5% dry milk in TBS-T for 1 h at RT. Following blocking, the membranes were incubated with primary antibodies in 5% BSA TBS overnight at 4°C (pEGFR at 1:1000 dilution, total EGFR 1:2000, PTPRJ, 1:200, β-Actin 1:4000). Membranes were then incubated with the appropriate secondary antibodies in TBS-T for 30 min at RT at 1:4000 dilution (Anti-rabbit: RRID:AB_2099233; Anti-mouse: RRID:AB_330924). Following washes with TBS-T, the immunoblot was visualized by chemiluminescence after incubation with Clarity Western ECL Substrate (Bio-Rad). Images were quantified using ImageJ (Abramoff, 2007) and plotted as normalized (ratio of phosphorylated to total intensity) mean values (Li et al., 2004; Russ & Engelman, 1999).

4.10 | Wound healing scratch assay

HSC3 cells were seeded in 6-well plates at a cell density necessary to reach confluency after 24 h and then serum-starved in serum-free media for 2 h before peptide treatment. Peptide preparation and cell treatment were performed as described above. After scratching the confluent cell monolayer with a 1 mL pipette tip, the media was replaced with complete media containing EGF (50 ng/mL) at 37°C for 10 h. Scratch areas were quantified with ImageJ using the *MRI Wound Healing Tool* (https://github.com/MontpellierRessourcesImagerie/imagej_macros_and_scripts/wiki/Wound-Healing-Tool), and the closure percent corresponds to the percent change in the area between the initial and final time points. Percent scratch closure was normalized to wild-type cells treated at pH 7.4.

4.11 | DN-AraTM assay

The DNA sequences coding for the TM domains of interest (see below) were subcloned into either pAraTMwt (coding for AraC) or pAraTMDN (coding for the inactive form of AraC, AraC*) plasmids, using standard molecular biology techniques. All constructs were verified by DNA sequencing.

PTPRJ QDPGVICGAVFGCIFGALVIVTVGGFIFW RKKRKDAKNNEVSFSQIKPK.

LTK KPPGPLVLMVAVVATSTLSLLMVCGVLILVKQ KKWQGLQEMRLPSPELE.

Hybrid7 DDTTLLLLSEIGAGMWVSLVELIADADEG.

Hybrid7-control DDTTLLLLSEIGLGMWVSLVELIA DADEG.

The AraC and AraC*-based plasmids were co-transformed with the reporter plasmid (pAraGFPCDF) into the AraC-deficient *E. coli* strain SB1676 (the *E. coli* Genetic Stock Center at Yale University) and streaked onto selective lysogeny broth (LB) plates (100 μg/mL ampicillin, 50 μg/mL kanamycin, and 100 μg/mL spectinomycin). Colonies were picked from each construct and tested, as previously described (Bloch et al., 2019). The results are reported as the ratio of GFP fluorescence emission at 530 nm to absorbance at 580 nm and normalized to the negative control (empty plasmids and reporter plasmid). Immunoblotting was performed using HRP-conjugated anti-Myc (1:5000; RRID:AB_2148465), and anti-HA (1:5000; RRID:AB_10978021) followed by secondary anti-mouse HRP-conjugated (1:5000; RRID:AB_330924).

4.12 | Peptide interaction with cells by fluorescence microscopy

HSC3 cells were seeded on 22 mm × 22 mm coverslips pretreated with poly-L-lysine in 6 well plates at 300,000 cells/well to be ~60% confluent after 16 h. Cells were treated for 10 min with 5 μM of FITC-hybrid7 as described above. Following two washes with PBS (same pH as treatment), the cells were fixed with non-permeabilizing 4% PFA in water for 10 min at 4°C. Fluorescence quenching was performed by treatment with 0.4% Trypan blue for 5 min. All samples were washed with PBS prior to mounting. The coverslips were mounted on slides with Fluoromount (Sigma-Aldrich #F4680) before being imaged by a Nikon Eclipse Ti microscope with a 20× objective.

4.13 | Peptide interaction with cells by flow cytometry

FITC-hybrid7 was solubilized in treatment media (supplemented with 10 mM sodium bicarbonate pH 7.4) to a final concentration of 1 μM. 300,000 HSC3 cells per sample were treated with peptides, washed, and fixed, as described above. After washing with PBS (pH 7.4), the samples were blocked with 1% BSA in PBS for 10 min at 4°C. The cells were labeled with 100 μL of anti-FITC-Alexa647 antibody (RRID:AB_2339044) in 1% BSA PBS (pH 7.4; final concentration of ~0.5 μg/mL) for 1 h at 4°C. After washing in PBS, samples without Trypan blue quenching were resuspended in PBS for analysis. Trypan blue samples were successively treated with 0.4% Trypan blue for 5 min before analysis. The cells were analyzed using a BDFacs Canto II flow cytometer equipped with a 488 nm argon laser with a 530/30 bandpass filter, and a 633 nm HeNe laser with a 660/20 bandpass filter. A minimum of 3000 events were counted for each experimental condition. The data were analyzed using FACSDiva. The fluorescence data are expressed as mean arbitrary fluorescence units and were gated to include all intact cells.

4.14 | Lactate dehydrogenase release assay

HSC3 cells were seeded in 24-well plates at 200,000 cells/well and incubated overnight at 37°C. The cells were then treated with 10 μM hybrid7 previously described for immunoblot analyses. The amount of lactate dehydrogenase (LDH) release was analyzed using the cyQUANT LDH Cytotoxicity assay (ThermoFisher, cat#C20301), as previously described (Gerhart et al., 2018). LDH release was normalized to cells treated with media only at pH 7.4 (spontaneous release) and cells lysed with the provided lysis buffer after treatment with media only at pH 7.4 (maximum release).

4.15 | Cell viability assay

HSC3 cells were seeded in 96-well plates at 5000 cells/well and incubated overnight at 37°C. The cells were treated with hybrid7 and hybrid7-control, prepared as previously described for immunoblot analyses. Following the treatment, the cells were washed once and then recovered in 100 μL of complete DMEM media for 72 h at 37°C. Cell viability was assessed via MTT assay, as previously reported (Bloch et al., 2019). Cell viability was normalized to cells treated with media only at pH 7.4 (100% viability). Data were fitted to a sigmoidal dose–response curve and EC50 values were determined using Prism 9 (GraphPad).

AUTHOR CONTRIBUTIONS

Sophie Rizzo: Investigation; methodology; validation; formal analysis; writing—review & editing; writing—original draft; data curation; visualization. **Eden Sikorski:** Investigation; writing—original draft; formal analysis; data curation; visualization; validation; methodology. **Soohyung Park:** Writing—review & editing; formal analysis; methodology; data curation; visualization; validation; investigation; software; funding acquisition. **Wonpil Im:** Writing—review & editing; formal analysis; software; methodology; validation; resources; supervision. **Victor Vasquez-Montes:** Data curation; methodology; formal analysis; validation; visualization; investigation. **Alexey S. Ladokhin:** Resources; supervision; methodology; writing—review & editing; formal analysis; validation; funding acquisition. **Damien Thévenin:** Conceptualization; funding acquisition; writing—review & editing; visualization; validation; methodology; formal analysis; project administration; resources; supervision.

ACKNOWLEDGMENTS

This work was supported by the National Institute of General Medical Sciences: R01GM139998 to Damien Thévenin and R01GM126778 to Alexey S. Ladokhin, and National Science Foundation MCB-2111728 to Wonpil Im.

ORCID

Victor Vasquez-Montes https://orcid.org/0000-0001-7593-7293

Damien Thévenin https://orcid.org/0000-0002-1866-0694

REFERENCES

Abramoff MD. ImageJ as an image processing tool and library. Microsc Microanal. 2007;13:1672–3.

Alves DS, Westerfield JM, Shi X, Nguyen VP, Stefanski KM, Booth KR, et al. A novel pH-dependent membrane peptide that binds to EphA2 and inhibits cell migration. ELife. 2018;7:e36645.

Åqvist J, Wennerström P, Nervall M, Bjelic S, Brandsdal BO. Molecular dynamics simulations of water and biomolecules with a Monte Carlo constant pressure algorithm. Chem Phys Lett. 2004;384:288–94.

Arora D, Stopp S, Böhmer S-A, Schons J, Godfrey R, Masson K, et al. Protein-tyrosine phosphatase DEP-1 controls receptor tyrosine kinase FLT3 signaling. J Biol Chem. 2011;286:10918–29.

Avraham R, Yarden Y. Feedback regulation of EGFR signalling: decision making by early and delayed loops. Nat Rev Mol Cell Biol. 2011;12:104–17.

Bañó-Polo M, Martínez-Gil L, Wallner B, Nieva JL, Elofsson A, Mingarro I. Charge pair interactions in transmembrane helices and turn propensity of the connecting sequence promote helical hairpin insertion. J Mol Biol. 2013;425:830–40.

Barr AJ, Ugochukwu E, Lee WH, King ONF, Filippakopoulos P, Alfano I, et al. Large-scale structural analysis of the classical human protein tyrosine phosphatome. Cell. 2009;136:352–63.

Barrera FN, Fendos J, Engelman DM. Membrane physical properties influence transmembrane helix formation. Proc Natl Acad Sci U S A. 2012;109:14422–7.

Barrera FN, Weerakkody D, Anderson M, Andreev OA, Reshetnyak YK, Engelman DM. Roles of carboxyl groups in the transmembrane insertion of peptides. J Mol Biol. 2011;413:359–71.

Barton R, Palacio D, Iovine MK, Berger BW. A cytosolic juxtamembrane interface modulates plexin a3 oligomerization and signal transduction. PloS One. 2015;10:e0116368.

Bhujwalla ZM, Artemov D, Ballesteros P, Cerdan S, Gillies RJ, Solaiyappan M. Combined vascular and extracellular pH imaging of solid tumors. NMR Biomed. 2002;15:114–9.

Bloch E, Sikorski EL, Pontoriero D, Day EK, Berger BW, Lazzara MJ, et al. Disrupting the transmembrane domain-mediated oligomerization of protein tyrosine phosphatase receptor J inhibits EGFR-driven cancer cell phenotypes. J Biol Chem. 2019;294:18796–806.

Böhmer S-A, Weibrecht I, Söderberg O, Böhmer F-D. Association of the protein-tyrosine phosphatase DEP-1 with its substrate FLT3 visualized by in situ proximity ligation assay das a, editor. PloS One. 2013;8:e62871.

Brooks BR, Brooks CL III, Mackerell AD Jr, Nilsson L, Petrella RJ, Roux B, et al. CHARMM: the biomolecular simulation program Brooks III CL, Case DA, editors. J Comput Chem. 2009;30:1545–614.

Bürck J, Wadhwani P, Fanghänel S, Ulrich AS. Oriented circular dichroism: a method to characterize membrane-active peptides in oriented lipid bilayers. Acc Chem Res. 2016;49:184–92.

Burns KE, Hensley H, Robinson MK, Thévenin D. Therapeutic efficacy of a family of pHLIP–MMAF conjugates in cancer cells and mouse models. Mol Pharm. 2017;14:415–22.

Burns KE, McCleerey TP, Thévenin D. pH-selective cytotoxicity of pHLIP-antimicrobial peptide conjugates. Sci Rep. 2016;6:28465.

Burns KE, Robinson MK, Thévenin D. Inhibition of cancer cell proliferation and breast tumor targeting of pHLIP–monomethyl auristatin E conjugates. Mol Pharm. 2015;12:1250–8.

Burns KE, Thévenin D. Down-regulation of PAR1 activity with a pHLIP-based allosteric antagonist induces cancer cell death. Biochem J. 2015;472:287–95.

Chen Y-H, Yang JT, Chau KH. Determination of the helix and β form of proteins in aqueous solution by circular dichroism. Biochemistry. 1974;13:3350–9.

Chow K-H, Ferguson DM. Isothermal-isobaric molecular dynamics simulations with Monte Carlo volume sampling. Comput Phys Commun. 1995;91:283–9.

Cohen P, Alessi DR. Kinase drug discovery—What's next in the field? ACS Chem Biol. 2013;8:96–104.

Cowen T, Haven AJ, Burnstock G. Pontamine sky blue: a counterstain for background autofluorescence in fluorescence and immunofluorescence histochemistry. Histochemistry. 1985;82:205–8.

Cunningham F, Deber CM. Optimizing synthesis and expression of transmembrane peptides and proteins. Methods. 2007;41:370–80.

Deng W, Cho S, Su P-C, Berger BW, Li R. Membrane-enabled dimerization of the intrinsically disordered cytoplasmic domain of ADAM10. Proc Natl Acad Sci. 2014;111:15987–92.

Eastman P, Swails J, Chodera JD, McGibbon RT, Zhao Y, Beauchamp KA, et al. OpenMM 7: rapid development of high performance algorithms for molecular dynamics gentleman R, editor. PLoS Comput Biol. 2017;13:e1005659.

Ercan D, Xu C, Yanagita M, Monast CS, Pratilas CA, Montero J, et al. Reactivation of ERK signaling causes resistance to EGFR kinase inhibitors. Cancer Discov. 2012;2:934–47.

Essmann U, Perera L, Berkowitz ML, Darden T, Lee H, Pedersen LG. A smooth particle mesh Ewald method. J Chem Phys. 1995;103:8577–93.

Farrington CC, Yuan E, Mazhar S, Izadmehr S, Hurst L, Allen-Petersen BL, et al. Protein phosphatase 2A activation as a therapeutic strategy for managing MYC-driven cancers. J Biol Chem. 2020;295:757–70.

Fendos J, Barrera FN, Engelman DM. Aspartate embedding depth affects pHLIP's insertion pKa. Biochemistry. 2013;52:4595–604.

Finger C, Escher C, Schneider D. The single transmembrane domains of human receptor tyrosine kinases encode self-interactions. Sci Signal. 2009;2:ra56.

Furcht CM, Muñoz Rojas AR, Nihalani D, Lazzara MJ. Diminished functional role and altered localization of SHP2 in non-small cell lung cancer cells with EGFR-activating mutations. Oncogene. 2013;32:2346–55.

Gao Y, Lee J, Smith IPS, Lee H, Kim S, Qi Y, et al. CHARMM-GUI supports hydrogen mass repartitioning and different protonation states of phosphates in lipopolysaccharides. J Chem Inf Model. 2021;61:831–9.

Gerhart J, Thévenin AF, Bloch E, King KE, Thévenin D. Inhibiting epidermal growth factor receptor dimerization and signaling through targeted delivery of a juxtamembrane domain peptide mimic. ACS Chem Biol. 2018;13:2623–32.

Gerweck LE, Seetharaman K. Cellular pH gradient in tumor versus normal tissue: potential exploitation for the treatment of cancer. Cancer Res. 1996;56:1194–8.

Goh ETH, Lin Z, Ahn BY, Lopes-Rodrigues V, Dang NH, Salim S, et al. A small molecule targeting the transmembrane domain of death receptor p75NTR induces melanoma cell death and reduces tumor growth. Cell Chem Biol. 2018;25:1485–94.

Gratkowski H, Lear JD, DeGrado WF. Polar side chains drive the association of model transmembrane peptides. Proc Natl Acad Sci U S A. 2001;98:880–5.

Hata AN, Niederst MJ, Archibald HL, Gomez-Caraballo M, Siddiqui FM, Mulvey HE, et al. Tumor cells can follow distinct evolutionary paths to become resistant to epidermal growth factor receptor inhibition. Nat Med. 2016;22:262–9.

He R, Yu Z, Zhang R, Zhang Z. Protein tyrosine phosphatases as potential therapeutic targets. Acta Pharmacol Sin. 2014;35:1227–46.

Hed J, Hallden G, Johansson SGO, Larsson P. The use of fluorescence quenching in flow cytofluorometry to measure the attachment and ingestion phases in phagocytosis in peripheral blood without prior cell separation. J Immunol Methods. 1987;101:119–25.

Hopkins CW, Le Grand S, Walker RC, Roitberg AE. Long-time-step molecular dynamics through hydrogen mass repartitioning. J Chem Theory Comput. 2015;11:1864–74.

Hower AE, Beltran PJ, Bixby JL. Dimerization of tyrosine phosphatase PTPRO decreases its activity and ability to inactivate TrkC. J Neurochem. 2009;110:1635–47.

Huang J, MacKerell AD. CHARMM36 all-atom additive protein force field: validation based on comparison to NMR data. J Comput Chem. 2013;34:2135–45.

Hunter T. Tyrosine phosphorylation: thirty years and counting. Curr Opin Cell Biol. 2009;21:140–6.

Im W, Lee MS, Brooks CL. Generalized born model with a simple smoothing function. J Comput Chem. 2003;24:1691–702.

Iuliano R, Le Pera I, Cristofaro C, Baudi F, Arturi F, Pallante P, et al. The tyrosine phosphatase PTPRJ/DEP-1 genotype affects thyroid carcinogenesis. Oncogene. 2004;23:8432–8.

Jandt E, Denner K, Kovalenko M, Östman A, Böhmer F-D. The protein-tyrosine phosphatase DEP-1 modulates growth factor-stimulated cell migration and cell–matrix adhesion. Oncogene. 2003;22:4175–85.

Jiang G, den Hertog J, Su J, Noel J, Sap J, Hunter T. Dimerization inhibits the activity of receptor-like protein-tyrosine phosphatase-α. Nature. 1999;401:606–10.

Jo S, Kim T, Iyer VG, Im W. CHARMM-GUI: a web-based graphical user interface for CHARMM. J Comput Chem. 2008;29:1859–65.

Jorgensen WL, Chandrasekhar J, Madura JD, Impey RW, Klein ML. Comparison of simple potential functions for simulating liquid water. J Chem Phys. 1983;79:926–35.

Keane MM, Lowrey GA, Ettenberg SA, Dayton MA, Lipkowitz S. The protein tyrosine phosphatase DEP-1 is induced during differentiation and inhibits growth of breast cancer cells. Cancer Res. 1996;56:4236–43.

Klauda JB, Venable RM, Freites JA, O'Connor JW, Tobias DJ, Mondragon-Ramirez C, et al. Update of the CHARMM all-atom additive force field for lipids: validation on six lipid types. J Phys Chem B. 2010;114:7830–43.

Kovalenko M, Denner K, Sandström J, Persson C, Groβ S, Jandt E, et al. Site-selective dephosphorylation of the platelet-derived growth factor β-receptor by the receptor-like protein-tyrosine phosphatase DEP-1. J Biol Chem. 2000;275:16219–26.

Kyrychenko A, Vasquez-Montes V, Ulmschneider MB, Ladokhin AS. Lipid headgroups modulate membrane insertion of pHLIP peptide. Biophys J. 2015;108:791–4.

Ladokhin AS, Jayasinghe S, White SH. How to measure and analyze tryptophan fluorescence in membranes properly, and why bother? Anal Biochem. 2000;285:235–45.

Lampugnani MG, Zanetti A, Corada M, Takahashi T, Balconi G, Breviario F, et al. Contact inhibition of VEGF-induced proliferation requires vascular endothelial cadherin, β-catenin, and the phosphatase DEP-1/CD148. J Cell Biol. 2003;161:793–804.

Lazzara MJ, Lane K, Chan R, Jasper PJ, Yaffe MB, Sorger PK, et al. Impaired SHP2-mediated extracellular signal-regulated kinase activation contributes to gefitinib sensitivity of lung cancer cells with epidermal growth factor receptor–activating mutations. Cancer Res. 2010;70:3843–50.

Lee J, Cheng X, Swails JM, Yeom MS, Eastman PK, Lemkul JA, et al. CHARMM-GUI input generator for NAMD, GROMACS, AMBER, OpenMM, and CHARMM/OpenMM simulations using the CHARMM36 additive force Field. J Chem Theory Comput. 2016;12:405–13.

Li R, Gorelik R, Nanda V, Law PB, Lear JD, DeGrado WF, et al. Dimerization of the transmembrane domain of integrin α_{IIb} subunit in cell membranes. J Biol Chem. 2004;279:26666–73.

Libermann TA, Nusbaum HR, Razon N, Kris R, Lax I, Soreq H, et al. Amplification, enhanced expression and possible rearrangement of EGF receptor gene in primary human brain tumours of glial origin. Nature. 1985;313:144–7.

MacKerell AD, Bashford D, Bellott M, Dunbrack RL, Evanseck JD, Field MJ, et al. All-atom empirical potential for molecular modeling and dynamics studies of proteins. J Phys Chem B. 1998;102:3586–616.

Manning G, Whyte DB, Martinez R, Hunter T, Sudarsanam S. The protein kinase complement of the human genome. Science. 2002;298:1912–34.

Melnyk RA, Partridge AW, Yip J, Wu Y, Goto NK, Deber CM. Polar residue tagging of transmembrane peptides. Biopolymers. 2003;71:675–85.

Mok TSK. Personalized medicine in lung cancer: what we need to know. Nat Rev Clin Oncol. 2011;8:661–8.

Musial-Siwek M, Karabadzhak A, Andreev OA, Reshetnyak YK, Engelman DM. Tuning the insertion properties of pHLIP. Biochim Biophys Acta. 2010;1798:1041–6.

Nguyen VP, Alves DS, Scott HL, Davis FL, Barrera FN. A novel soluble peptide with pH-responsive membrane insertion. Biochemistry. 2015;54:6567–75.

Niederst MJ, Engelman JA. Bypass mechanisms of resistance to receptor tyrosine kinase inhibition in lung cancer. Sci Signal. 2013;6:re6. https://doi.org/10.1126/scisignal.2004652

Nunes-Xavier CE, Martín-Pérez J, Elson A, Pulido R. Protein tyrosine phosphatases as novel targets in breast cancer therapy. Biochim Biophys Acta. 2013;1836:211–26.

Onyango JO, Chung MS, Eng C-H, Klees LM, Langenbacher R, Yao L, et al. Noncanonical amino acids to improve the pH response of pHLIP insertion at tumor acidity. Angew Chem Int Ed Engl. 2015;54:3658–63.

Palka HL, Park M, Tonks NK. Hepatocyte growth factor receptor tyrosine kinase met is a substrate of the receptor protein-tyrosine phosphatase DEP-1. J Biol Chem. 2003;278:5728–35.

Patel JP, Gönen M, Figueroa ME, Fernandez H, Sun Z, Racevskis J, et al. Prognostic relevance of integrated genetic profiling in acute myeloid leukemia. N Engl J Med. 2012;366:1079–89.

Petermann A, Haase D, Wetzel A, Balavenkatraman KK, Tenev T, Gührs K-H, et al. Loss of the protein-tyrosine phosphatase DEP-1/PTPRJ drives meningioma cell motility: regulation of meningioma cell-motility by DEP-1. Brain Pathol. 2011;21:405–18.

Ruivenkamp C, Hermsen M, Postma C, Klous A, Baak J, Meijer G, et al. LOH of PTPRJ occurs early in colorectal cancer and is associated with chromosomal loss of 18q12-21. Oncogene. 2003;22:3472–4.

Ruivenkamp CAL, van Wezel T, Zanon C, Stassen APM, Vlcek C, Csikós T, et al. Ptprj is a candidate for the mouse colon-cancer susceptibility locus Scc1 and is frequently deleted in human cancers. Nat Genet. 2002;31:295–300.

Russ WP, Engelman DM. TOXCAT: a measure of transmembrane helix association in a biological membrane. Proc Natl Acad Sci U S A. 1999;96:863–8.

Ryckaert J-P, Ciccotti G, Berendsen HJC. Numerical integration of the cartesian equations of motion of a system with constraints: molecular dynamics of n-alkanes. J Comput Phys. 1977;23:327–41.
Schwarz M, Rizzo S, Paz WE, Kresinsky A, Thévenin D, Müller JP. Disrupting PTPRJ transmembrane-mediated oligomerization counteracts oncogenic receptor tyrosine kinase FLT3 ITD. Front Oncol. 2022;12:1017947.
Spano J-P, Lagorce C, Atlan D, Milano G, Domont J, Benamouzig R, et al. Impact of EGFR expression on colorectal cancer patient prognosis and survival. Ann Oncol. 2005;16:102–8.
Steinbach PJ, Brooks BR. New spherical-cutoff methods for long-range forces in macromolecular simulation. J Comput Chem. 1994;15:667–83.
Su P-C, Berger BW. Identifying key juxtamembrane interactions in cell membranes using AraC-based transcriptional reporter assay (AraTM). J Biol Chem. 2012;287:31515–26.
Su P-C, Berger BW. A novel assay for assessing juxtamembrane and transmembrane domain interactions important for receptor heterodimerization. J Mol Biol. 2013;425:4652–8.
Sugita Y, Okamoto Y. Replica-exchange molecular dynamics method for protein folding. Chem Phys Lett. 1999;314:141–51.
Tarcic G, Boguslavsky SK, Wakim J, Kiuchi T, Liu A, Reinitz F, et al. An unbiased screen identifies DEP-1 tumor suppressor as a phosphatase controlling EGFR endocytosis. Curr Biol. 2009;19:1788–98.
Tonks NK. Protein tyrosine phosphatases—from housekeeping enzymes to master regulators of signal transduction. FEBS J. 2013;280:346–78.
Ubersax JA, Ferrell JE Jr. Mechanisms of specificity in protein phosphorylation. Nat Rev Mol Cell Biol. 2007;8:530–41.
Van Amersfoort ES, Van Strijp JAG. Evaluation of a flow cytometric fluorescence quenching assay of phagocytosis of sensitized sheep erythrocytes by polymorphonuclear leukocytes. Cytometry. 1994;17:294–301.
Vasquez-Montes V, Gerhart J, King KE, Thévenin D, Ladokhin AS. Comparison of lipid-dependent bilayer insertion of pHLIP and its P20G variant. Biochim Biophys Acta. 2018;1860:534–43.
Vasquez-Montes V, Gerhart J, Thévenin D, Ladokhin AS. Divalent cations and lipid composition modulate membrane insertion and cancer-targeting action of pHLIP. J Mol Biol. 2019;431:5004–18.
Vasquez-Montes V, Tyagi V, Sikorski E, Kyrychenko A, Freites JA, Thévenin D, et al. Ca $^{2+}$-dependent interactions between lipids and the tumor-targeting peptide pHLIP. Protein Sci. 2022;31:e4385. https://doi.org/10.1002/pro.4385
Vaupel P, Kallinowski F, Okunieff P. Blood flow, oxygen and nutrient supply, and metabolic microenvironment of human tumors: a review. Cancer Res. 1989;49:6449–65.
Warburg O. On the origin of cancer cells. Science. 1956;123:309–14.
Wehr J, Sikorski EL, Bloch E, Feigman MS, Ferraro NJ, Baybutt TR, et al. pH-dependent grafting of cancer cells with antigenic epitopes promotes selective antibody-mediated cytotoxicity. J Med Chem. 2020;63:3713–22.
Wike-Hooley JL, Haveman J, Reinhold HS. The relevance of tumour pH to the treatment of malignant disease. Radiother Oncol. 1984;2:343–66.
Wimley WC, White SH. Designing transmembrane α-helices that insert spontaneously. Biochemistry. 2000;39:4432–42.
Wonganu B, Berger BW. A specific, transmembrane interface regulates fibroblast activation protein (FAP) homodimerization, trafficking and exopeptidase activity. Biochim Biophys Acta. 2016;1858:1876–82.
Woodcock HL, Hodošček M, Gilbert ATB, Gill PMW, Schaefer HF, Brooks BR. Interfacing Q-chem and CHARMM to perform QM/MM reaction path calculations: interfacing Q-chem and CHARMM to perform QM/MM reaction path calculations. J Comput Chem. 2007;28:1485–502.
Wu EL, Cheng X, Jo S, Rui H, Song KC, Dávila-Contreras EM, et al. CHARMM-GUI *membrane builder* toward realistic biological membrane simulations. J Comput Chem. 2014;35:1997–2004.
Wu Y, Huang HW, Olah GA. Method of oriented circular dichroism. Biophys J. 1990;57:797–806.
Zhang X, Lin Y, Gillies RJ. Tumor pH and its measurement. J Nucl Med. 2010;51:1167–70.
Zhou FX, Merianos HJ, Brunger AT, Engelman DM. Polar residues drive association of polyleucine transmembrane helices. Proc Natl Acad Sci U S A. 2001;98:2250–5.

SUPPORTING INFORMATION

Additional supporting information can be found online in the Supporting Information section at the end of this article.

How to cite this article: Rizzo S, Sikorski E, Park S, Im W, Vasquez-Montes V, Ladokhin AS, et al. Promoting the activity of a receptor tyrosine phosphatase with a novel pH-responsive transmembrane agonist inhibits cancer-associated phenotypes. Protein Science. 2023;32(9):e4742. https://doi.org/10.1002/pro.4742